Unsteady flow in a channel obstructed by a square rod (crisscross motion of vortex)

Hiroshi Suzuki, Yoshiaki Inoue, Toshihiko Nishimura, Kazuhisa Fukutani, and Kenjiro Suzuki
Department of Mechanical Engineering, Kyoto University, Kyoto, Japan

A two-dimensional numerical computation was made for unsteady laminar flow in a channel obstructed with a square rod placed perpendicular to the flow in the channel center plane. The computation was made for several cases of different rod sizes, different Reynolds numbers, and different patterns of inlet flow velocity profiles. The vortex shedding frequency and the drag coefficient of the rod are discussed first. Then the behavior of the vortex street formed downstream of the rod is discussed in particular. The present computation reveals that the vortex street shows a different pattern of motion from its counterpart formed behind a rod placed in a uniform flow. In several cases of obstructed channel flow, it is found that vortices that are shed from the upper half of the rod cross the channel center plane toward the bottom channel wall as they move downstream, and those that are shed from the lower half of the rod move toward the upper half of the flow space. Flow visualization was made for the flow in a channel obstructed by a square rod and confirmed the appearance of this interesting crisscross motion of the vortices. The blockage ratio is indicated to be a major factor governing the conditions for the appearance of the crisscross motion of the vortex. Misalignment of the rod position leading to asymmetry of flow is found to cause no serious suppression of the crisscross motion of the vortex.

Keywords: unsteady channel flow; numerical analysis; obstruction with a square rod; vortex street; flow visualization; Strouhal number; crisscross motion of vortex

Introduction

Recently, periodically changing laminar unsteady flows have been attracting much attention. These types of unsteady flows appear in practical heat transfer devices in the transitional Reynolds number range. It is known that heat transfer can be enhanced by the incipience of flow instability (Nishihara, Suzuki, and Inoue 1988; Xi et al. 1989). However, the mechanism of heat transfer under such unsteady flow conditions has not been studied sufficiently. Periodically changing unsteady flow is particularly interesting because its periodical nature provides better conditions to facilitate the analysis of the heat transfer mechanism in an unsteady flow condition. In this article, attention is paid to a flow to be generated in a channel behind a square rod mounted in its center plane, and numerical computation is made for several cases of such an obstructed channel flow. A two-dimensional (2-D) treatment will be used in the present numerical analysis, taking a similar standpoint to that of Karniadakis, Mikic, and Patera (1988) and Davis and Moore (1982). This flow situation is related to another practical application of the vortex-shedding flow meter. The case in which the inlet flow has a parabolic velocity profile will be treated as the basic case in this study. Characteristics of the flow behind the rod are discussed, based on the results of a numerical computation. Special attention will be paid to a newly found crisscross motion of the vortex or the difference in the flow behavior between the basic case and the case when a rod is located in a uniform flow. Results of some flow visualizations that confirm the numerical results will also be reported. Effects of the blockage ratio and displacement of the rod position from the channel center plane on the appearance of the crisscross motion of vortex will also be discussed.

Address reprint requests to Professor H. Suzuki at the Department of Mechanical Engineering, Kyoto University, Kyoto 606, Japan.

Received 11 February 1991; accepted 30 March 1992

Procedure of numerical computation

The finite-difference equivalents of the 2-D, time-dependent momentum equations were numerically solved with a computer. Constant properties were assumed for the working fluid. Under that assumption, the momentum equations are written as follows:

$$\frac{\partial}{\partial t}(\rho U)+\frac{\partial}{\partial x}(\rho U^2)+\frac{\partial}{\partial y}(\rho VU) = -\frac{\partial P}{\partial x}+\frac{\partial}{\partial x}\left(\mu\frac{\partial U}{\partial x}\right)+\frac{\partial}{\partial y}\left(\mu\frac{\partial U}{\partial y}\right) \quad (1)$$

$$\frac{\partial}{\partial t}(\rho V)+\frac{\partial}{\partial x}(\rho UV)+\frac{\partial}{\partial y}(\rho V^2) = -\frac{\partial P}{\partial y}+\frac{\partial}{\partial x}\left(\mu\frac{\partial V}{\partial x}\right)+\frac{\partial}{\partial y}\left(\mu\frac{\partial V}{\partial y}\right) \quad (2)$$

For finite differencing of the convection terms, a third-order upwind scheme (QUICK) (see Leonard 1979) was applied, while central finite differencing was used for the diffusion terms. Fully implicit forms of the finite-difference equations obtained were solved successively from one time to another step by step. The time increment between two successive time steps was set so that the Courant number for the smallest grid spacing

evaluated with the cross-sectional average velocity, U_m, was unity. An iterative procedure was adopted in the calculation at each time step to correct the solution for the pressure field so as to match the updated velocity field. The alternating direction implicit (ADI) method was combined in the iterative procedure. The pressure field was calculated by following the pressure correction method, i.e., SIMPLE (see Patankar and Spalding 1972).

Figure 1 schematically shows the computational domain. The streamwise length of the domain was set equal to $12H$, where H is the width of the channel, and a square rod was located at a position $2H$ downstream from the upstream end of the computational domain. The streamwise and normal coordinates were designated by x and y, respectively, and the origin of the coordinate system was located at the center of the rod. The computation was made for six different sizes of rod; $d = 0.5H$, $0.4H$, $0.3H$, $0.2H$, $0.1H$, and $0.05H$. Except for some cases for which computations were made in preliminary and supplemental studies to be briefly discussed later, all other computational conditions treated in the present study are tabulated in Table 1. At the upstream boundary, the inlet flow was assumed to be steady and hydrodynamically fully developed, i.e., characterized by a parabolic inlet velocity profile for cases A through L. The inlet flow for the other two cases, M and N, was assumed to have a uniform velocity profile. Another computation was made for a channel flow of reversed parabolic velocity profile and cross-sectional average velocity U_m (case O). This is an artificial case introduced just for comparison, but it may correspond to the case where the channel walls slide at a constant velocity ($2U_m$) under the pressure gradient to keep the cross-sectional average velocity U_m. One more computation was made for the flow behind a square rod located in a uniform flow in an infinitely large space (case P).

The channel Reynolds number, Re, based on the hydraulic equivalent diameter of the channel ($2H$) and on the cross-sectional average velocity, U_m, was held constant at 1,000 for cases A, D, and G. On the other hand, in cases J, K, and L, the rod Reynolds number, Re_d, based on the rod size, d, was kept constant at the same value of 150 as in the cases of A, M, O, and P. In preliminary study, additional computations were made for the case in which the rod was located in a uniform flow in an infinitely large space, in order to confirm the validity of the computation to be discussed below. In such computations,

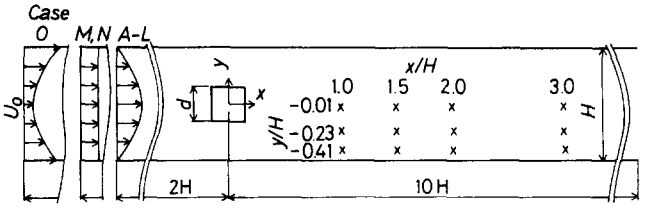

Figure 1 Computational domain

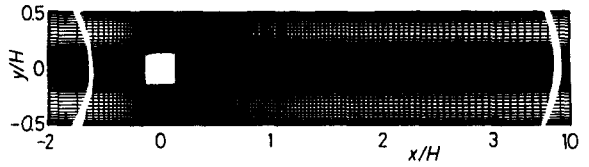

Figure 2 Grid system

Re_d was changed from 150 in several steps. In the cases of $d/H = 0.05$, 0.1, 0.2, and 0.3, computations were added for the cases of the channel Reynolds number lower than those tabulated in Table 1, but it was found that the flow in such cases remains to be steady laminar, as will be discussed later. Additional computations were also made for the cases when the rod was placed off the central plane. In such computations, the channel Reynolds number was kept constant at 1,000 and the blockage ratio d/H was set equal to 0.3. The results of these computations will also be discussed later.

A total of 207 × 54 grid points were allocated nonuniformly in the computational domain, as shown in Figure 2 for case A; the finest arrangement of grid points was close to the edges of the rod, where the streamlines are expected to intersect at the largest angle (on average) with the direction of grid point alignment.

A no-slip condition was applied as the velocity boundary condition along the solid wall. The flow field at the downstream end of the computational domain was treated so as to obey the boundary-layer approximation (Suzuki et al. 1981; Suzuki 1990). The computation was started with an imaginary flow

Notation

C_p	Pressure coefficient $(2(P - P_0)/\rho U_m^2)$
C_D	Drag coefficient $(2D/\rho U_m^2 d)$
C_D^*	Drag coefficient based on U^* $(2D/\rho U_m^2 d)$
d	Size of a square rod, m
D	Drag force per unit length, N/m
e	Distance between the rod center and the channel center plane, m
f	Frequency, Hz
H	Distance between two parallel flat plates, m
P	Pressure, Pa
P_u	One-sided power spectra of u, m^2/s
Re	Channel Reynolds number $(2\rho U_m H/\mu)$
Re_d	Rod Reynolds number $(\rho U_m d/\mu)$
Re_d^*	Rod Reynolds number based on U^* $(\rho U^* d/\mu)$
Re_g	Grid Reynolds number $(\rho U_m \Delta x_{min}/\mu)$
S	Nondimensional frequency (fd/U_m)
St	Strouhal number $(\omega d/2\pi U_m)$
St*	Strouhal number based on U^* $(\omega d/2\pi U_m)$
t	Time, s
U	Streamwise velocity, m/s
U^*	Mean velocity in the clearance $(U_m/(1 - d/H))$, m/s
u	Fluctuating streamwise velocity, m/s
V	Normal velocity, m/s
x	Streamwise distance from the center of a rod, m
y	Normal distance from the center of a rod, m

Greek symbols

Δx_{min}	Minimum grid spacing, m
μ	Viscosity of fluid, Pa·s
ρ	Density of fluid, kg/m^3
ω	Angular frequency of Karman vortex, rad/s

Subscripts and superscripts

m	Cross-sectional mean
0	Inlet
′	Intensity (root mean square value)

Table 1 Flow conditions, Strouhal number, and drag coefficient

Case	d/H	Inlet condition	Re	Re_d	Re_d^*	St	St*	C_D	C_D^*
A	0.3	Fully developed	1,000	150	214	0.324	0.227	4.36	2.14
B	0.3	Fully developed	700	105	150	0.322	0.225	4.15	2.03
C	0.3	Fully developed	600	90	129	0.312	0.218	4.23	2.07
*	1/4	Fully developed	1,000	125	167	0.192	0.144	3.34	1.88
D	0.2	Fully developed	1,000	100	125	0.222	0.178	3.49	2.21
E	0.2	Fully developed	700	70	88	0.221	0.177	3.46	2.21
F	0.2	Fully developed	600	60	75	0.215	0.172	3.38	2.16
*	1/6	Fully developed	1,000	83	100	0.175	0.146	3.13	2.18
G	0.1	Fully developed	1,000	50	55.6	0.167	0.150	3.16	2.56
H	0.05	Fully developed	2,000	50	52.6	0.166	0.158	3.06	2.76
I	0.05	Fully developed	1,500	37.5	39.5	0.152	0.144	3.10	2.80
J	0.5	Fully developed	600	150	300	0.519	0.260	8.17	2.04
K	0.4	Fully developed	750	150	250	0.440	0.264	5.27	1.90
L	0.2	Fully developed	1,500	150	187.5	0.199	0.159	3.69	2.36
M	0.3	Uniform flow	1,000	150	214	0.321	0.225	3.25	1.59
*	1/4	Uniform flow	1,000	125	167	0.200	0.15	2.82	1.59
#	0.2		1,000	100	125	0.15	0.12	—	—
*	1/6	Uniform flow	1,000	83	100	0.161	0.134	2.32	1.61
N	0.1	Uniform flow	1,000	50	55.6	0.145	0.131	2.20	1.78
O	0.3	Moving walls	1,000	150	214	0.206	0.144	1.60	0.78
P	—	Uniform free flow	—	150	—	0.143	—	1.54	—

*Values taken from Davis, Moore, and Purtell (1984).
#Values taken from Ohwa, Sakao, and Matsuoka (1988).
$U^* = U_m/(1 - d/H)$; $Re_d^* = Re_d(U^*/U_m) = Re_d/(1 - d/H)$; $St^* = St(U_m/U^*) = St(1 - d/H)$; $C_D^* = C_D(U_m^2/U^{*2}) = C_D(1 - d/H)^2$.

field as the initial condition and proceeded step by step while the fluctuating manner of the flow was monitored. The results were examined for cycles long after the Karman vortex-shedding frequency had reached an asymptotic value. Several different flow fields were tested as the initial conditions, and the results obtained at such an asymptotic condition were confirmed to agree well with each other. The results to be discussed later were obtained with an initial condition such that the velocity profile at the inlet was assigned to all the streamwise cross sections except for the sections corresponding to the space between the square rod and the channel walls, where a modification of the velocity profile was made to satisfy overall mass continuity.

Experimental apparatus

An open water channel described in Yao, Nakatani, and Suzuki (1989) was used for flow visualization. Figure 3 illustrates the experimental apparatus. An overflow tank was used to keep the water head constant so that the flow was kept steady at the inlet of the test section. The channel Reynolds number, Re, was set equal to 1,000. The rod (size $0.3H$) was positioned vertically in the center plane of the channel (width $H = 50$ mm).

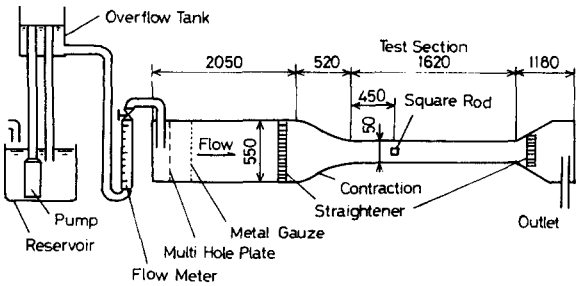

Figure 3 Experimental apparatus

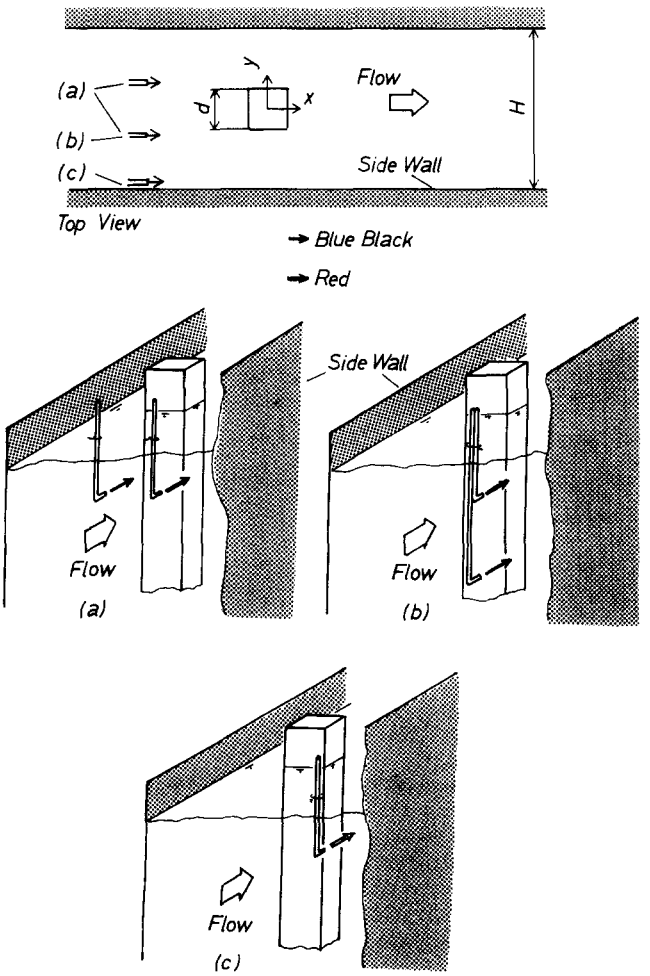

Figure 4 Position of injection needles: (a) for flow visualization of Karman vortex street; (b) for flow visualization of flow two-dimensionality; and (c) for flow visualization of near wall region

However, the channel length was not long enough to locate the rod at a place where the flow would be fully developed. Thus, the results of the flow visualization are compared with the numerical results of cases A and M for different inlet velocity profiles.

Series of photographs were taken from the top at intervals of about half a second by making use of a still camera with an automatic shutter, which was located in a position looking down the flow in the channel at a distance of about one meter from the flow area to be visualized. The period of incurred unsteady flow was observed to be about four seconds. Therefore, eight photographs could be taken in one cycle of flow fluctuation. Three different kinds of flow visualization were carried out. In two of them, the flow behind the rod was visualized, and in another, visualization was made for flow behavior near the channel wall. For the first two purposes, two thin injection needles having an inner diameter of 0.5 mm were placed about 20 mm apart from each other at a streamwise position just upstream of the rod, and two different colors of dye (red and blue-black) were, respectively, injected downstream from them. In order to visualize the behavior of Karman vortex, the two injection needles were positioned in the manner illustrated in Figure 4a. For the purpose of observing the two-dimensionality of the flow, they were positioned in another manner, illustrated in Figure 4b. Finally, for the purpose of visualizing the near wall flow behavior, one injection needle was placed near the wall in a manner illustrated in Figure 4c.

Results and discussions

To check the effect of grid spacing, computations were performed for case A with four different grid systems, tabulated in Table 2. Figure 5 shows the dependency of the observed Strouhal number on the grid spacing. The abscissa of the figure is the grid Reynolds number, Re_g, based on the minimum grid spacing and on the cross-sectional average velocity. The horizontal line in the figure indicates the Strouhal number (0.33) obtained in the present flow visualization. The results obtained with grid systems p3 and p4 agree fairly well with each other. Finer grid spacing may give a more accurate solution; however, refinement of the accuracy of computation will be small after the number of grid points is increased beyond a certain level. At the same time, computational cost becomes larger. In the present computation, the p3 grid system or its equivalents were adopted based on the trade-off between the accuracy and the cost of the computation. The Strouhal number numerically obtained with the grid system p3 is close to the Strouhal number obtained in the flow visualization. Inlet flow was not in a fully developed state in the flow visualization, as was assumed in the computation. However, as will be found later, the value of the Strouhal number evaluated with U_m is rather insensitive to the difference of the shape of the approaching flow velocity profile. These facts provide evidence for the validity of the present computational procedure and the adopted grid spacing. In relation to the discussion below, it is observed that the Strouhal number is calculated to be smaller with coarser grid systems. This is found in the results of other investigators (Davis and Moore 1982).

Table 2 System of grid points (case A)

Case	Grid points	Re_g	CPU time*
p1	131 × 26	18.8	0.17
p2	159 × 36	12.5	0.35
p3	207 × 54	6.8	1
p4	244 × 70	4.7	2.63

* CPU time is described in a form normalized by the one required in the computation with the grid arrangement p3.

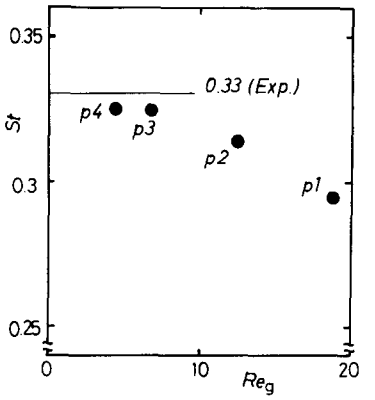

Figure 5 Strouhal number for each grid system

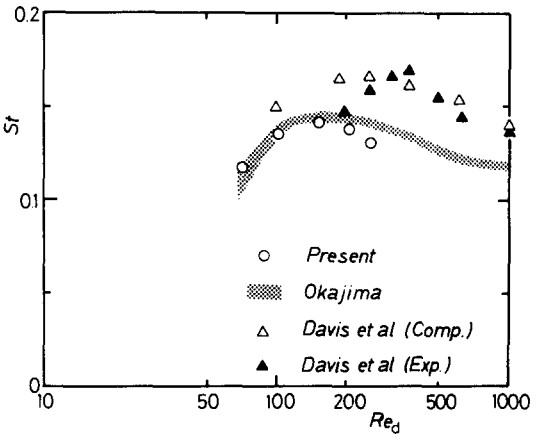

Figure 6 Strouhal number in uniform flow

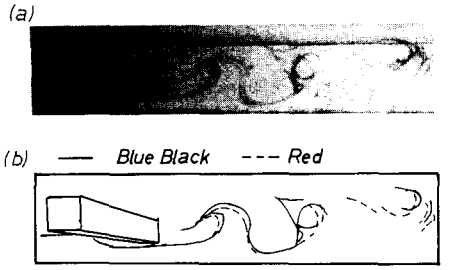

Figure 7 Flow visualization of flow two-dimensionality, $d/H = 0.3$: (a) photograph; and (b) sketch

Another preliminary examination was made for the cases when a square rod was located in a uniform flow in order to confirm the validity of the present computational procedure. The rod Reynolds number, Re_d, was changed in five steps, i.e., $Re_d = 70$, 100, 150 (case P), 200, and 250. Figure 6 shows the Strouhal numbers obtained numerically for these cases in comparison with the experimental data by Okajima (1982) (shown as shaded region in the figure), Davis and Moore (1982), and also with the numerical results by Davis et al. (1984). The discrepancy observed between the two sets of experimental data was simply attributed to the difference in the main flow

turbulence level (Davis et al. 1984). However, there may be some other factors causing such discrepancy, like rod end-effect and sharpness of the rod edges. The present numerical results are close to the experimental data by Okajima (1982), particularly in the range of the rod Reynolds number (less than 150), for which the present numerical computation of obstructed channel flow was made. This fact also suggests the validity of the present computational procedure.

Figure 7a shows a black-and-white copy of the colored photograph obtained in the flow visualization carried out with an arrangement of dye injection needles illustrated in Figure 4b. Figure 7b is a sketch to supplement the photograph. From the photograph and its sketch, both lines are observed to be almost included in the same vertical sheet of fluid. Additionally, when both lines are viewed horizontally, it was observed that they keep almost the same spanwise positions as they flow downstream. Therefore, the flow presently studied is confirmed to be essentially 2-D, at least in the region covered by the photograph ($1 < x/H < 3$) at the Reynolds number 1,000.

Figure 8 shows an example of the instantaneous contours of vorticity for each of the cases A through I, and Figure 9 illustrates similar instantaneous vorticity contours for each of the cases J through P. Shaded and unshaded areas shown in

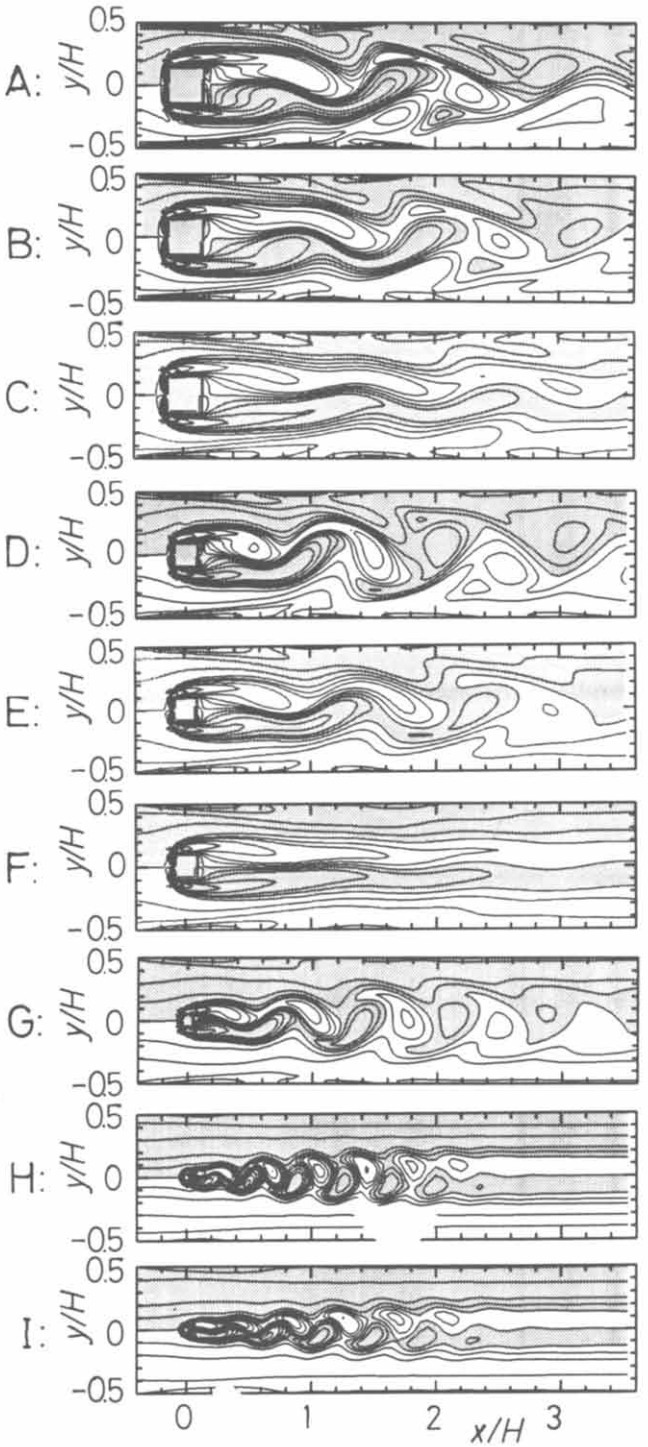

Figure 8 Instantaneous vorticity contours (case A through I)

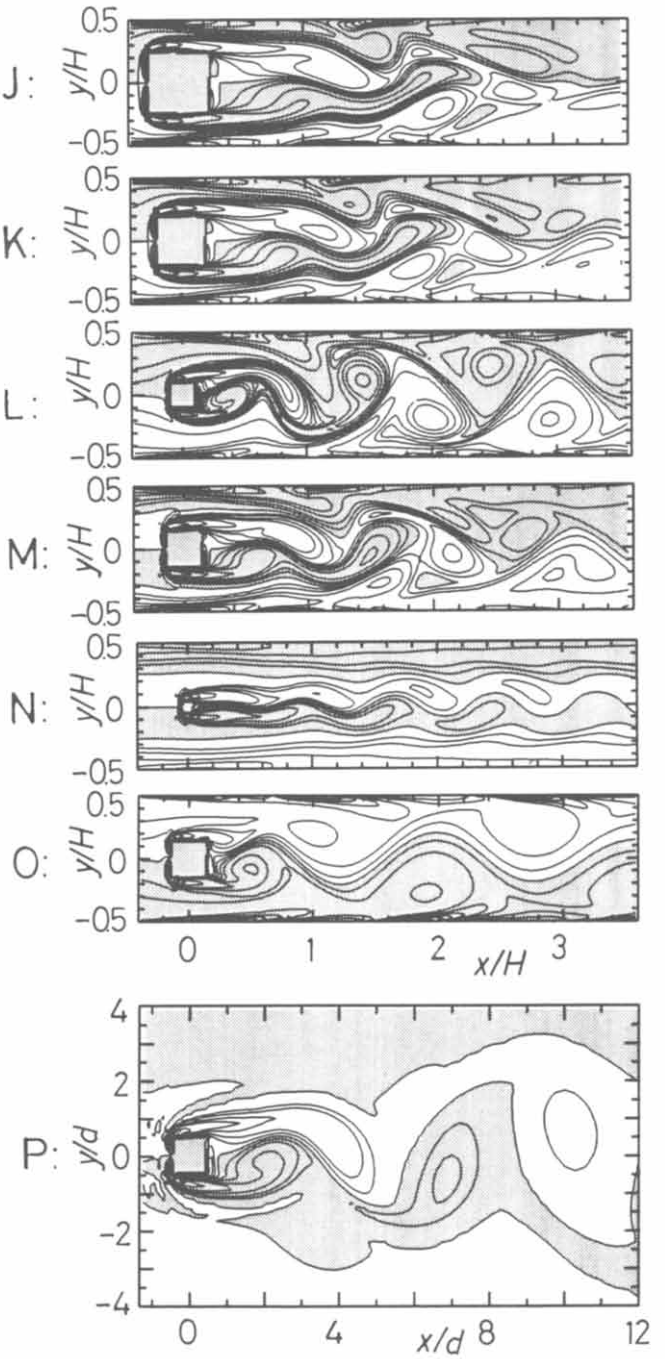

Figure 9 Instantaneous vorticity contours (case J through P)

these figures correspond, respectively, to the areas where the instantaneous vorticity takes positive and negative values. In all cases except for case F, periodical shedding of the Karman vortex is clearly observed.

Figure 10 shows some examples of frequency spectra of the streamwise velocity fluctuation obtained from numerical results for case A at 6 of the 12 locations identified in Figure 1. They indicate that the calculated velocity fluctuation is highly periodic and is composed of harmonics. Thus, the calculated unsteady flow is found not to be irregular. Therefore, it is concluded to be different from turbulent flow, which is characterized by irregularity in time and space. The present type of unsteady flow may be called laminar unsteady flow.

The Strouhal number and drag coefficient obtained for each case are listed in Table 1. The Strouhal number, St, and the drag coefficient were defined with the cross-sectional mean velocity, U_m, in the present study. In order to take into account the effect of the space between the rod and the channel wall, the Strouhal number, St*, and drag coefficient, C_D^*, defined with the mean velocity of the flow through the clearance between the rod and the wall, U^*, are also listed in Table 1. In the table, some numerical results reported by Davis, Moore, and Purtell (1984) and by Ohwa, Sakao, and Matsuoka (1988) for similar flow situations were included for comparison. As seen in the table, the Strouhal number does not take the same value along the studied cases, due to the difference in the rod Reynolds number and in the blockage ratio d/H. In contrast to those effects, the effect of approaching flow velocity profile is minor. The results of Davis, Moore, and Purtell (1984) are observed to be a little lower than the present results. The results of Ohwa, Sakao, and Matsuoka (1988) are also found to be noticeably lower than the present results. One of the reasons for this difference, judged from Figure 5, is that finer grid spacing was used in the present study. Figure 11 presents the calculated Strouhal numbers, St and St*, together with some other data (Davis, Moore, and Purtell 1984; Ohwa, Sakao, and Matsuoka 1988; Blot et al. 1989). The present results, if plotted in the form of St*, lie rather close to the data of Blot et al. (1989) for the turbulent flow regime. The drag coefficient also does not take the same value among the cases of different blockage ratio, even if Re_d is kept constant; it increases with an increase of d/H, as seen from the comparison of the results among cases A, J, K, and L. The values of C_D^* become closer to the values for the case in which the rod is located in a uniform flow in an infinitely large space, and they are also found to vary less conspicuously with the blockage ratio.

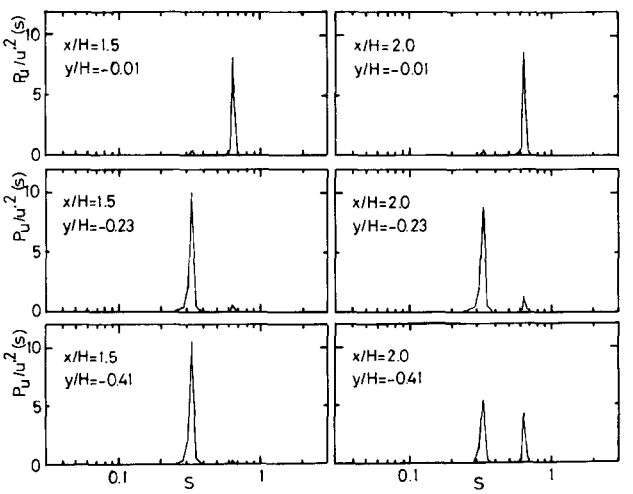

Figure 10 Power spectra of fluctuating velocity for case A

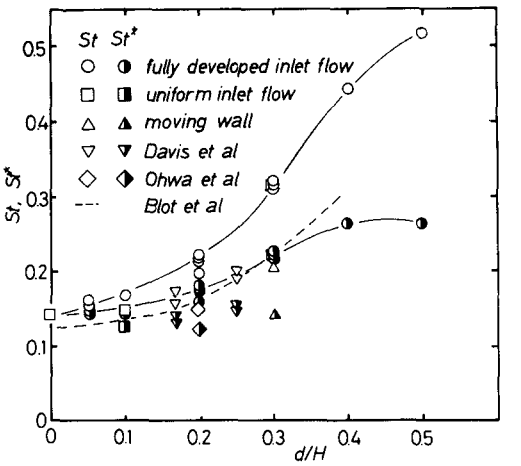

Figure 11 Change of Strouhal number with blockage ratio

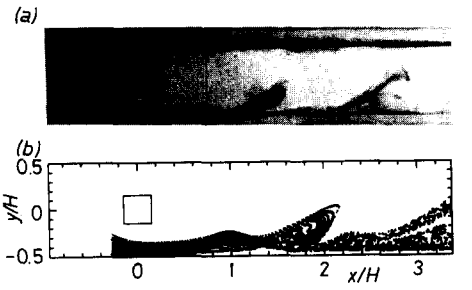

Figure 12 Flow visualization of near wall region, $d/H = 0.3$: (a) photograph; and (b) instantaneous streak lines for case A

In many cases, as illustrated in Figures 8 and 9, it is observed that the near wall region is noticeably affected by the Karman vortex and that the near wall flow becomes also unsteady. To confirm this, another type of flow visualization was made with a single dye-injection needle arranged in the manner shown in Figure 4c. The obtained photograph is shown in Figure 12a. Figure 12b shows the streak lines calculated at an instant for case A. Similarity of behavior is obvious between the visualized and calculated streak lines, and the unsteady behavior of the near-wall flow was actually confirmed. As for the disturbance generated in the near wall region, a noticeable difference is observed between cases A and G ($d/H = 0.3$ and $d/H = 0.1$, respectively). In the latter case, conspicuous time-dependent fluid motion is only noticeable in the core region, and the flow in the region close to the channel wall behaves in a manner rather close to the one observed for steady flow regime. In other words, disturbance created in the near wall region by the insertion of the rod is much less significant when d/H is as small as 0.1. On the other hand, the wall region is noticeably disturbed by the periodically appearing Karman vortices in the case of $d/H = 0.3$. This difference results in a level of periodic change of instantaneous wall heat transfer characteristics (Suzuki and Suzuki, forthcoming).

In Figures 8 and 9, it is also noticeable in case P that the vortex having positive vorticity remains in the lower half of the domain and that the one having a negative sign remains in the upper half of the domain; namely, each vortex remains on the same side in which it was originally shed. An important point to be noted is that there is a clear difference in the motion of the shed vortices between case P and case A. In the latter case,

a vortex does not remain on the same side from which it was originally shed. The vortex shed from the upper half of the rod gradually moves toward the bottom wall of the channel as it flows downstream, and the vortex shed from the lower half moves toward the top wall. This clearly differs from the vortex observable in case P, when the rod is located in a uniform unconfined flow. The same thing is observed in all of the other cases B through M except for cases C, F, H, and I. In case C, no crisscross motion is observed in the region shown in Figure 8 but is confirmed to occur at positions of $x/H > 3.6$. In case F, flow is unsteady. However, only the wavy motion of the separation layer is observed, and the Karman vortex does not appear. This case will be discussed again later.

In order to confirm this numerical result, flow visualization was performed in a flow similar to the presently calculated one using the open channel described above. In this flow visualization, the two injection needles of dye were positioned in the manner illustrated in Figure 4a. Figure 13a shows one of the photographs taken in such a flow visualization for the case in which $d/H = 0.3$. To supplement the black-and-white copy of the colored photograph, a sketch of the photograph is added in Figure 13b. It is clearly observed that the vortex shed from the lower side of the rod moves toward the top wall of the channel and that the one from the upper side of the rod crosses the center plane towards the bottom wall of the channel. The numerical results for case A shown in Figure 8 are not the streak lines observed in flow visualization but rather vorticity contours. Comparison of the results of cases A and M reveals that the velocity profile of the flow approaching the rod does not noticeably alter the pattern of the vortex motion. Therefore, for direct comparison, the streak lines obtained from the numerical results for case A are shown in Figure 13c. For simplicity in this figure, only the streak lines passing below the rod are shown. They are found to behave similarly to those actually observed in the flow visualization. Therefore, the peculiar crisscross motion of Karman vortices found in the present numerical computation has been confirmed to actually exist. This agreement also confirms the validity of the 2-D treatment of the flow and of the adopted numerical procedure, at least, in the region of $x/H < 3.5$ at the Reynolds number of 1,000.

In order to present an idea about the condition necessary for the appearance of the crisscross motion of the Karman vortex, numerical computation was supplementarily added for several other cases just to see when flow becomes unsteady and if Karman vortices show crisscross motion. These computations

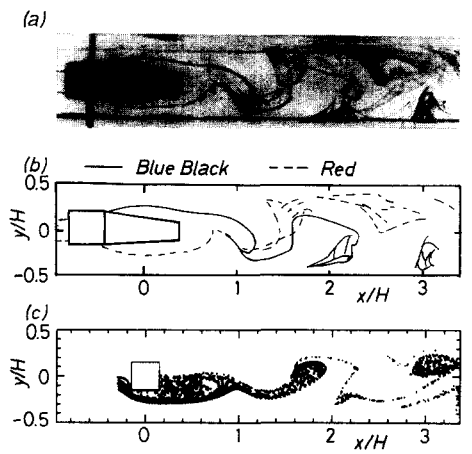

Figure 13 Results of flow visualization, $d/H = 0.3$: (a) photograph; (b) sketch; and (c) instantaneous streak lines for case A

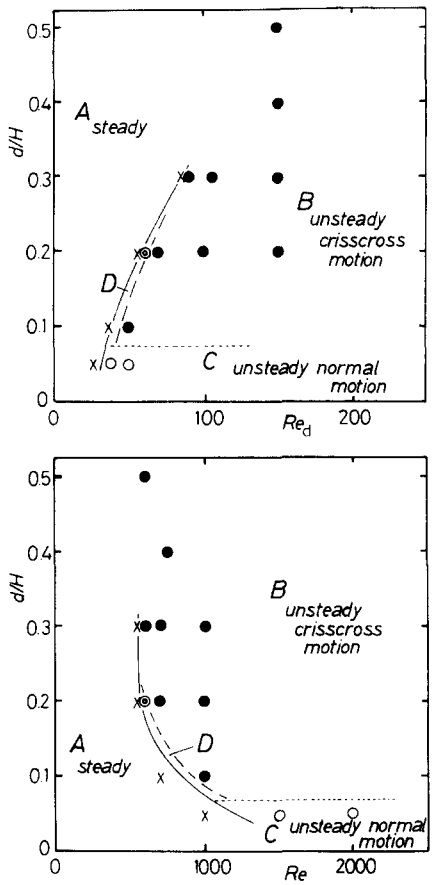

Figure 14 Map for occurrence of crisscross motion of vortex: (a) steady flow; (b) unsteady flow—Karman vortex shows crisscross motion; (c) unsteady flow—Karman vortex shows normal motion; and (d) unsteady, but Karman vortex is not shed

were made assuming the inlet velocity profile to be parabolic. Figure 14 presents a map of the obtained results. In this map, the results of the cases tabulated in Table 1 were also included.

It is found in this figure that whenever the Karman vortex appears at all the blockage ratios of $d/H \geqslant 0.1$, the crisscross motion of vortex is generated. However, at the smallest blockage ratio of $d/H = 0.05$, the Karman vortex shows normal behavior. Therefore, the blockage ratio is a major factor governing whether the Karman vortex shows crisscross motion or not. At a blockage ratio larger than 0.1, the crisscross motion of the vortex appears at any Reynolds number at which flow instability occurs. Thus, the presence of the wall near the vortex is a very important condition for the appearance of the crisscross motion of the vortex. However, in case N (where the blockage ratio is the same as that for case C, namely, $d/H = 0.1$), it is found that the vortices do not show crisscross motion. This suggests that the effect of the wall on whether the crisscross motion of the vortices occurs or not is not simple. It should be studied in detail, with attention paid to the time variation of instantaneous flow structure. This will be done in Suzuki et al. (forthcoming).

It is also observed in Figure 14 that a critical Reynolds number for flow instability depends on the blockage ratio. The critical value of the rod Reynolds number increases with an increase in the blockage ratio, but the critical value of the channel Reynolds number is lowered with an increase in the blockage ratio.

One more examination was made to clarify how the

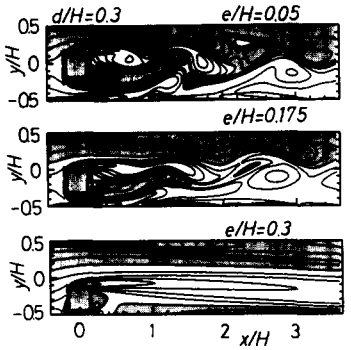

Figure 15 Instantaneous vorticity contours; cases when the rod ($d/H = 0.3$) is mounted off the channel center plane

misalignment of a rod leading to the asymmetry of flow affects the appearance of the crisscross motion of the vortex. For this purpose, another computation was added to the other three cases of $d/H = 0.3$ and $e/H = 0.05$, 0.175, and 0.3, where e is the distance between the rod center and the channel center plane. Instantaneous vorticity contours obtained for the three cases are shown as examples in Figure 15. In the case of $e/H = 0.3$, in which the space between the rod and the channel wall is as small as $0.05H$, the vortices are not shed periodically. In the case of $e/H = 0.175$, the vortices that are shed from the lower side of the rod disappear quickly but still show crisscross motion. Therefore, asymmetry of the flow geometry does not sensitively affect the appearance or nonappearance of the crisscross motion of the vortex.

Concluding remarks

Numerical computations were made for channel flows that were hydrodynamically fully developed at the inlet but were obstructed by a square rod placed perpendicular to the flow direction in the channel center plane. In two exceptional computations, uniform flow was assumed to exist at the inlet. Several other computations were added for cases in which the rod was placed in a uniform unconfined flow, channel walls slid at a constant speed, and the rod was placed off its center plane in a channel. Computation was made for various sizes of rod and at different channel and rod Reynolds numbers. The validity of the present 2-D computation was confirmed by comparing the numerical results for the obstructed channel flow and the wake behind a square rod placed in a uniform unconfined flow with corresponding experimental results. It was demonstrated that vortices shed from the rod can behave differently in the two cases of confined flow and unconfined flow. Numerical results for channel flows show that vortices cross from one half of the flow space to another in some cases of obstructed channel flow. This was confirmed by the flow visualization. The blockage ratio or the presence of channel walls is concluded to be the major factor determining whether the crisscross motion of the vortex is generated or not. Asymmetry of the flow caused by the misposition of the rod is found not to seriously affect the condition of whether the vortex exhibits crisscross motion or not.

Acknowledgment

Acknowledgment by the authors is extended to the partial support of this study given through the Grant in Aid of Scientific Research of the Ministry of Education, Science and Culture, Japan, No. 01603523.

References

Blot, F., Giovannini, A., Hebrard, P., and Strzelecki, A. 1989. Flow analysis in a vortex flowmeter: an experimental and numerical approach. *Proc. 7th Symp. Turbulent Shear Flows*, 10.3.1–10.3.5, Stanford

Davis, R. W. and Moore, E. F. 1982. A numerical study of vortex shedding from rectangles. *J. Fluid Mech.*, **116**, 475–506

Davis, R. W., Moore, E. F., and Purtell, L. P. 1984. A numerical-experimental study of confined flow around rectangular cylinders. *Phys. Fluids*, **27**(1), 46–59

Karniadakis, G. E., Mikic, B. B., and Patera, A. T. 1988. Minimum-dissipation transport enhancement by flow destabilization: Reynolds' analogy revisited. *J. Fluid Mech.*, **192**, 365–391

Leonard, B. P. 1979. A stable and accurate convective modelling procedure based on quadratic interpolation. *Comput. Methods Appl. Mech. Eng.*, **19**, 59–98

Nishihara, A., Suzuki, K., and Inoue, Y. 1988. Numerical computation of flow and heat transfer in a channel with a sudden expansion. *Proc. Natl. Heat Transfer Symp. Jpn.*, **2**, 76–78 (in Japanese)

Ohwa, Y., Sakao, F., and Matsuoka, Y. 1988. Numerical analysis of non-constant flow around a rectangular cylinder between parallel walls. *Trans. JSME*, **54**(498), 277–281

Okajima, A. 1982. Strouhal numbers of rectangular cylinders. *J. Fluid Mech.*, **123**, 379–398

Patankar, S. V. and Spalding, D. B. 1972. A calculation procedure for heat, mass and momentum transfer in three-dimensional parabolic flows. *Int. J. Heat Mass Transfer*, **15**, 1787–1806

Suzuki, K., Kieda, S., Chichiki, T., and Sato, T. 1981. Numerical study of combined convective heat transfer with variable fluid properties in the inlet region of a circular tube. In *Numerical Methods in Laminar and Turbulent Flow*, Lewis, R. W., et al. (eds.). Pinneridge Press, Swansea, 1048–1059

Suzuki, H. 1990. Study on heat transfer under an unsteady flow obstructed by a cylindrical body. Doctoral thesis, Kyoto University (in Japanese)

Suzuki, K. and Suzuki, H. Forthcoming. Unsteady flow heat transfer in a channel obstructed with an immersed body. In *Annual Review of Heat Transfer*, Tien, C. L., (ed.), Vol. 5., Begell House, New York

Suzuki, K., et al. Submitted. Instantaneous structure and statistical feature of unsteady flow in a channel obstructed by a square rod

Xi, G. N., Suzuki, K., Hagiwara, Y., and Murata, T. 1989. A basic study on heat transfer characteristics of offset fin arrays—effect of fin thickness in the middle range of Reynolds number. *Trans. JSME Ser. B*, **55**(519), 3507–3514 (in Japanese)

Yao, M., Nakatani, M., and Suzuki, K. 1989. Flow visualization and heat transfer experiments in a duct with a staggered array of cylinders. *Exp. Thermal Fluid Sci.*, **2**, 193–200